catalysts

MDPI

Article

Engineering Oxygen Vacancies in Pt/TiO_2 Catalysts for Efficient Light-Driven Reverse Water-Gas Shift

Li Fang, Yuxian Jiang, Xueyang Jiang, Qin Zhang, Sihui Suo, Chenhui Zhao, Jiayu Song and Jiancong Liu *

Key Laboratory of Functional Inorganic Material Chemistry, Ministry of Education of the People's Republic of China, Heilongjiang University, Harbin 150080, China

* Correspondence: liujiancong@hlju.edu.cn or jiancong@gmail.com

Abstract

Oxygen vacancies are a key factor determining the efficiency of the CO_2 hydrogenation reaction and play a crucial role in CO_2 adsorption and activation. However, effectively regulating the concentration of oxygen vacancies to enhance the performance of the light-driven reverse water gas shift (RWGS) reaction remains a challenge. To address this, this study successfully developed Pt/TiO_2 catalysts with varying oxygen vacancy concentrations by controlling the morphology of TiO_2. Structural characterization results indicate that, compared to Pt/TiO_2-NR, Pt/TiO_2-NB exhibits a higher oxygen vacancy (O_V) concentration and greater CO_2 absorption. Catalytic performance evaluation results showed that under an irradiance of 2.5 W/cm^2, the CO production rates of the Pt/TiO_2-NB catalyst reached 57.03 mol·g_{Pt}^{-1}·h^{-1}. Furthermore, the catalyst maintained excellent catalytic stability during 45 h of continuous operation, demonstrating good potential for practical applications.

Keywords: morphology modulation; Pt/TiO_2; light-driven; reverse water gas shift; oxygen vacancies

1. Introduction

With the rapid depletion of fossil fuels, atmospheric CO_2 concentrations continue to rise, triggering global climate change. The catalytic conversion of CO_2 into high-value chemicals or fuels is viewed as a dual strategy to mitigate both the energy crisis and the greenhouse effect [1–3]. However, due to the high bond dissociation energy of the C=O bond (approximately 750 kJ mol^{-1}), high operating temperatures and pressures are typically required to achieve effective CO_2 conversion [4–6]. To this end, diverse catalytic technologies, including electrocatalysis, photocatalysis, and thermocatalysis, have been extensively explored [7]. Typically, photothermal catalysis has emerged as a transformative alternative that uniquely integrates solar-driven photochemical charge separation with thermochemical conversion pathways. This synergy enables the reverse water-gas shift (RWGS) reaction ($CO_2 + H_2 \rightarrow CO + H_2O$, $\Delta H = +41.2$ kJ·mol^{-1}) to proceed under significantly milder conditions, circumventing the high external energy input and catalyst deactivation issues typical of conventional thermocatalysis [8–10]. For this promising technology, the critical bottleneck is developing catalysts that efficiently couple light harvesting, charge separation, and surface redox reactions. Among them, TiO_2-supported metal catalysts are at the forefront, but their photothermal RWGS efficiency remains heavily governed by the concentration of oxygen vacancies.

Surface and interface engineering, particularly the introduction of oxygen vacancies (O_V), is a cornerstone strategy for enhancing light-driven catalyst performance [11,12]. The

Academic Editor: Giuseppe Mele

Received: 25 May 2026
Revised: 24 June 2026
Accepted: 4 July 2026
Published: 7 July 2026

introduction of O_V not only enhances the adsorption and activation of CO_2 molecules but also improves the material's own photothermal response capability [13,14]. Therefore, changes in oxygen vacancy concentration significantly influence the overall catalytic performance of light-driven CO_2 hydrogenation. Among the numerous oxide supports, TiO_2 demonstrates unique application potential due to its moderate band structure, chemical stability, and susceptibility to surface defect formation. These characteristics enable it not only to accommodate and stabilize oxygen vacancies but also to interact effectively with photogenerated charge carriers, making it an ideal catalyst for light-driven catalytic systems [15,16]. However, pure TiO_2 exhibits significant limitations in H_2 dissociation. This issue can be addressed by loading precious metals, which form Schottky junctions with the support to facilitate electron transport. Additionally, these metals provide active sites, thereby enhancing H_2 dissociation and CO_2 activation capabilities and inducing the formation of more oxygen vacancies [17–19]. While extensive efforts have focused on introducing O_V through heteroatom doping, precious metals loading or constructing metal-oxide heterojunctions, a question remains largely unexplored: Can the intrinsic morphology of the TiO_2 support itself be exploited as a design parameter to precisely control O_V generation?

Based on this, this study prepared TiO_2 carriers with two morphologies—nanobipyramids and nanorods—using different synthesis methods, and further loaded them with Pt to construct two catalysts: Pt/TiO_2-NB and Pt/TiO_2-NR. This work presents a systematic investigation that directly links TiO_2 morphology to oxygen vacancy formation and the resulting light-driven RWGS performance, an aspect that has rarely been explored previously. Unlike conventional studies that focus solely on Pt particle size or metal-support interactions, our work reveals that the nanobipyramid structure is more susceptible to H_2 reduction, generating a higher concentration of O_V compared to the nanorods. Structural characterization indicates that Pt/TiO_2-NB exhibits a higher O_V concentration compared to Pt/TiO_2-NR. Catalytic performance evaluation demonstrates that under an irradiance of 2.5 W/cm^2, the CO production rate of Pt/TiO_2-NB reaches 57.03 mol·g_{Pt}^{-1}·h^{-1}, with excellent stability maintained over 45 h of continuous operation. These findings not only provide a new design strategy for developing highly efficient photothermal CO_2 hydrogenation catalysts, but also offer fundamental insights into morphology-dependent defect engineering in TiO_2-based catalytic systems.

2. Results

2.1. Characterization of Pt/TiO_2 Composite Catalysts

To investigate the structural characteristics of the two catalysts with different morphologies, X-ray diffraction (XRD) analysis was performed to characterize their crystalline phases, and the results are shown in Figure 1a. The synthesized samples exhibited diffraction peaks at 25.28°, 37.80°, 48.05°, and 55.06°, corresponding to the (101), (004), (200), and (211) crystal planes of the TiO_2 anatase phase (JCPDS No. 21-1272) [20], respectively. No characteristic peaks attributable to rutile phases were detected, confirming the phase purity of the synthesized TiO_2. Notably, no characteristic peaks of metallic Pt were detected in the diffraction pattern, suggesting that metallic Pt is highly dispersed on the support surface. The structural properties of the synthesized samples were investigated via N_2 adsorption–desorption measurements, as shown in Figure 1b, Figures S1 and S2 and Table S1. The surface areas of Pt/TiO_2-NB and Pt/TiO_2-NR were 110.24 m^2 g^{-1}, and 109.93 m^2 g^{-1}, respectively. A high specific surface area not only facilitates metal dispersion but also provides more gas adsorption sites. In particular, for CO_2 adsorption, a high-surface-area support can host more basic sites or oxygen vacancies, thereby significantly enhancing the CO_2 adsorption capacity.

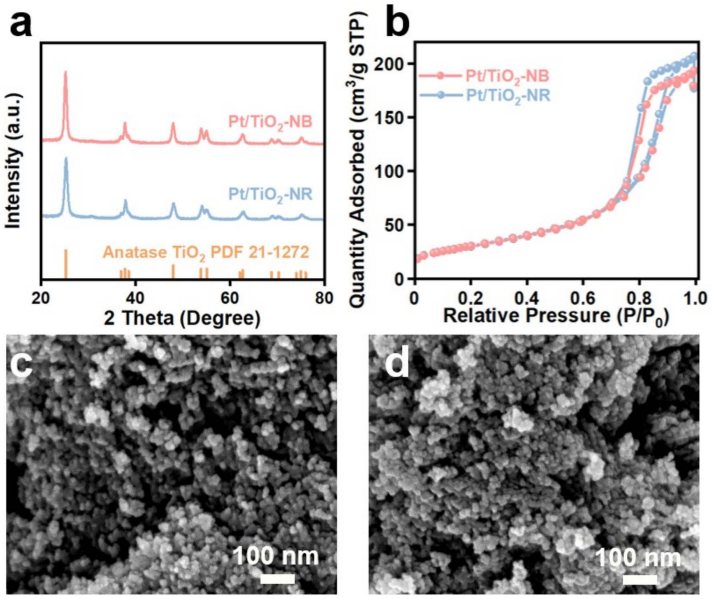

Figure 1. (**a**) XRD patterns of Pt/TiO_2-NB and Pt/TiO_2-NR. (**b**) N_2 adsorption–desorption isotherms of Pt/TiO_2-NB and Pt/TiO_2-NR. (**c**) SEM image of Pt/TiO_2-NB. (**d**) SEM image of Pt/TiO_2-NR.

Scanning Electron Microscopy (SEM) analysis provides a preliminary view of the overall morphology of the Pt/ TiO_2-NB and Pt/TiO_2-NR samples. As shown in Figure 1c,d, both samples consist of nanoparticles with a uniform distribution; no obvious large aggregates or single crystals were observed, and the samples exhibit the characteristics of nanocrystals [21]. Specifically, the particle size of Pt/TiO_2-NB is approximately 20 nm, while that of Pt/TiO_2-NR ranges between 20 and 30 nm. This highly dispersed, small-sized carrier helps generate more active sites on the surface, maximizes the exposure of active sites, and may promote synergistic interactions between the carrier and the active component. Due to the small size of the samples, Transmission Electron Microscopy (TEM) was employed for further detailed structural characterization. As shown in Figure 2a, Pt/TiO_2-NB exhibits a nanobipyramids morphology with a lattice fringe spacing of approximately 0.35 nm, corresponding to the (101) crystal plane of anatase TiO_2 [22], which is consistent with the XRD results. As shown in Figure 2b, Pt particles are uniformly dispersed on the TiO_2 surface. It is worth noting that due to the crystal extinction behavior of anatase TiO_2 and the preferential orientation effect of nanorods, the diffraction peak of the (100) crystal plane is extremely weak in conventional XRD patterns; therefore, TEM is required to provide more intuitive evidence. As shown in Figure 2c,d, Pt/TiO_2-NR exhibits a nanorod morphology with Pt uniformly loaded onto the carrier surface. Clear lattice striations are visible, with an interplanar spacing of approximately 0.19 nm, corresponding to the (100) crystal plane of anatase TiO_2 [23,24]. Combining the SEM and TEM characterization results confirms that TiO_2 with different morphologies has been successfully synthesized, and that different morphologies expose different preferred crystal planes, with metallic Pt uniformly loaded onto the carrier surface. The Pt particle size distribution analysis (Figure 2e,f) reveals that the mean diameters of Pt nanoparticles in Pt/TiO_2-NB and Pt/TiO_2-NR are 1.11 nm and 1.08 nm, respectively, suggesting that the Pt dispersion is essentially comparable across both samples.

To comprehensively evaluate the reduction performance of different catalysts, H_2 temperature-programmed reduction (H_2-TPR) tests were conducted on each sample; the results are shown in Figure 3a. The TPR curves of all catalysts exhibited two major reduction peaks. The low-temperature peak at approximately 100 °C can be attributed to the reduction of surface PtO_X species to metallic Pt^0. In the high-temperature region,

both catalysts exhibited a reduction peak attributable to the reduction of Ti^{4+} on the support surface to Ti^{3+}. The reduction temperature of Pt/TiO_2-NB in this region was lower than that of Pt/TiO_2-NR, indicating that the former favors the formation of more oxygen vacancies [25,26], which serve as CO_2 adsorption sites to enhance the activity of the light-driven RWGS reaction. Notably, when compared with the bare TiO_2 support, the high-temperature reduction peak of Pt/TiO_2-NB is substantially shifted to a lower temperature (376.8 °C vs. 483.8 °C, Figure S3). This marked decrease suggests that Pt may facilitate the reduction of TiO_2, possibly through promoted H_2 dissociation and hydrogen spillover. To further verify the O_V concentration, the O_V of the catalyst was characterized using Electron Paramagnetic Resonance (EPR), as shown in Figure 3b. Compared to Pt/TiO_2-NR, Pt/TiO_2-NB exhibited a stronger EPR signal at g = 2.001 [27]. This indicates that the surface of Pt/TiO_2-NB contains more oxygen vacancies than that of Pt/TiO_2-NR, consistent with the TPR results. Analysis of O_V via X-ray photoelectron spectroscopy (XPS), as shown in Figure 3c, revealed that the peak at 529.7 eV corresponds to lattice oxygen (O_L), the peak at 530.5 eV originates from chemically adsorbed oxygen species at O_V, and the peak at 532.0 eV stems from O_{OH} [4,28]. It can be observed that the O_V/O_L ratio of Pt/TiO_2-NB (0.25) is higher than that of Pt/TiO_2-NR (0.20). This indicates a high concentration of O_V on the Pt/TiO_2-NB catalyst. The adsorption of CO_2 on Pt/TiO_2-NB and Pt/TiO_2-NR was further investigated using CO_2-TPD (Figure S4). The adsorption intensity of CO_2 on the Pt/TiO_2-NB sample was higher than that on the Pt/TiO_2-NR sample, following the same order as the O_V concentration, indicating that a higher O_V concentration promotes CO_2 adsorption [29]. Additionally, the XPS spectra of the Ti 2p orbitals were analyzed. As shown in Figure 3d, the Ti 2p XPS spectrum reveals two pairs of peaks at 458.5 and 464.2 eV, corresponding to Ti^{4+} $2p_3/_2$ and Ti^{4+} $2p_1/_2$ [30], while the other two peaks at 462.8 and 457.4 eV originate from the Ti^{3+} $2p_1/_2$ and Ti^{3+} $2p_3/_2$ states [31], respectively. Both catalysts exhibit four peaks, indicating that a portion of Ti^{4+} has been reduced to Ti^{3+}, and the peak area of Ti^{3+} in the Pt/TiO_2-NB sample is larger than that in the Pt/TiO_2-NR sample.

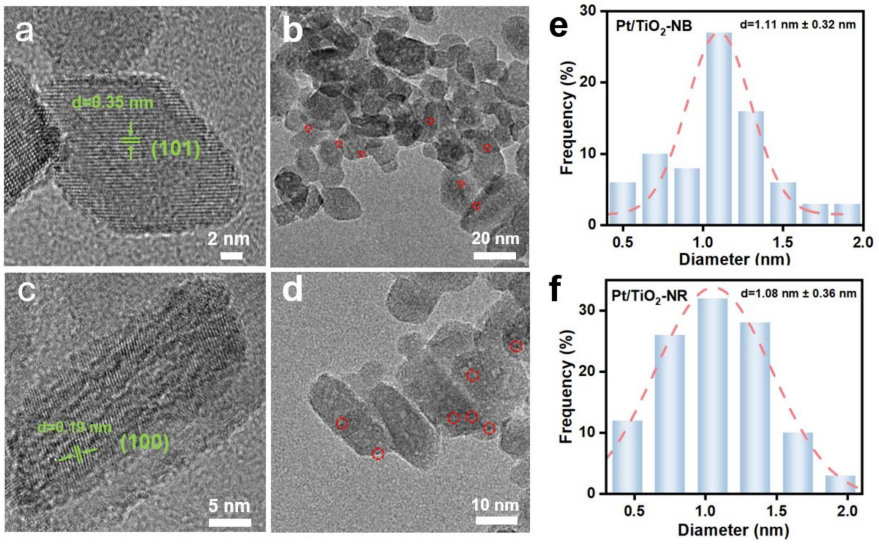

Figure 2. (**a**,**b**) TEM images of Pt/TiO_2-NB (Pt particles are circled in red). (**c**,**d**) TEM images of Pt/TiO_2-NR (Pt particles are circled in red). (**e**,**f**) Particle size distribution of Pt in Pt/TiO_2-NB and Pt/TiO_2-NR (mean ± standard deviation).

To investigate the Pt loading content in the catalysts, Inductively Coupled Plasma Optical Emission Spectroscopy (ICP-OES) analysis was performed on both catalysts. The data are presented in Table S2, showing that the actual Pt loading in both catalysts is similar. Since the Pt loading in the two catalysts is similar, X-ray photoelectron spectroscopy (XPS)

was used to further determine the state of Pt species in the catalysts and to investigate the electronic structure of Pt on Pt/TiO_2-NB and Pt/TiO_2-NR. As shown in Figure 3e, both the Pt/TiO_2-NB and Pt/TiO_2-NR catalysts exhibit three pairs of peaks, corresponding to the Pt^0 (70.6/73.8 eV), Pt^{2+} (72.2/75.7 eV), and Pt^{4+} (74.8/78.0 eV) species [32,33]. Typically, Pt^0 species originate from Pt clusters or nanoparticles, while Pt^{2+} and Pt^{4+} species are associated with Pt-O-Ti species at the Pt/TiO_2 interface. The data in the figure show that both catalysts are dominated by Pt^{2+} species. However, it is worth noting that the peak area contribution of the Pt^{2+} species on the Pt/TiO_2-NB catalyst was 0.81, while that on the Pt/TiO_2-NR catalyst was 0.78, demonstrating that the catalysts do not agglomerate after high-temperature reduction. Due to the unique structure of the precious metal catalyst, metallic Pt can further enhance the hydrogen dissociation process. As shown in Figure 3f, H_2 temperature-programmed desorption (H_2-TPD) tests were conducted using equal amounts of catalyst. The H_2-TPD curve consists of two regions: the low-temperature desorption peak is assigned to hydrogen species adsorbed on Pt sites (Pt-H), and the high-temperature desorption peak corresponds to hydrogen species that have migrated to the TiO_2 support (spillover H) [33,34]. It can be observed that the high-temperature desorption peak of Pt/TiO_2-NB is higher than that of Pt/TiO_2-NR. This result is primarily attributed to enhanced desorption of spillover H species. This indicates that the Pt/TiO_2-NB catalyst exhibits a stronger hydrogen spillover effect.

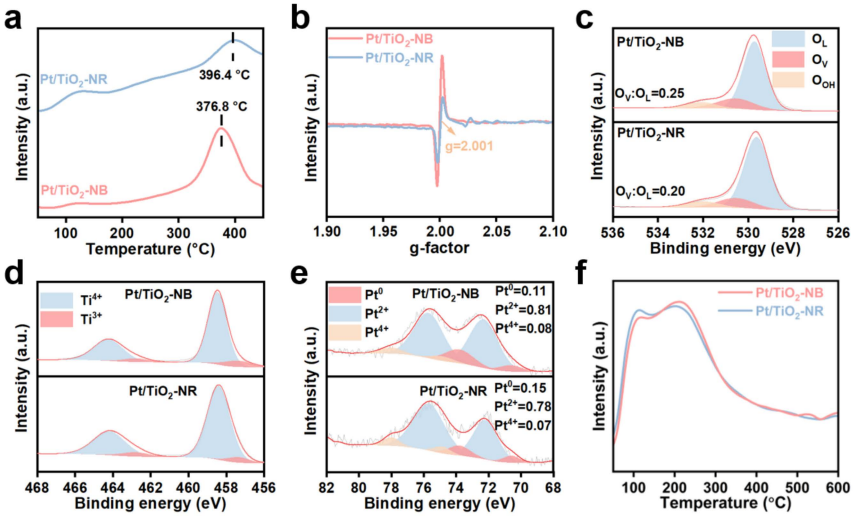

Figure 3. Characterization of Pt/TiO_2-NB and Pt/TiO_2-NR: (**a**) H_2-TPR curves, (**b**) EPR spectra, (**c**) O 1S XPS spectra, (**d**) Ti 2p XPS spectra, (**e**) Pt 4f XPS spectra, and (**f**) H_2-TPD curves.

2.2. Bandgap of Pt/TiO_2 Composite Catalysts

As shown in Figure 4a, the light absorption characteristics of the catalyst were characterized using UV-Vis absorption spectroscopy (UV-Vis) diffuse reflectance spectroscopy. Compared to Pt/TiO_2-NR, Pt/TiO_2-NB exhibits a better response to visible light, with its light absorption range extending from the UV to the visible region, indicating higher efficiency in utilizing sunlight. The bandgap of Pt/TiO_2-NB was calculated using the Tuac method to be 2.09 eV, which is narrower than that of Pt/TiO_2-NR (2.31 eV). This narrowing is attributed to the higher concentration of O_V in Pt/TiO_2-NB, which introduces defect states within the TiO_2 bandgap. The narrowed bandgap facilitates the absorption of visible light and generation of more photo-generated carriers under visible light irradiation, which is crucial for achieving highly efficient light-driven catalysis. Furthermore, XPS valence band (VB) spectra were used to determine the VB positions of Pt/TiO_2-NB and Pt/TiO_2-NR. As shown in Figure 4b, the VB of Pt/TiO_2-NB (1.45 eV) is lower than that of Pt/TiO_2-NR (1.74 eV). By combining UV-Vis diffuse reflectance spectroscopy and valence band X-ray

photoelectron spectroscopy (VB-XPS) data, complete band structure diagrams for the two samples were plotted, as shown in Figure 4c. The conduction band (CB) potentials of both catalysts were below the standard thermodynamic potential for CO_2 reduction to CO (−0.53 eV), indicating that both possess sufficient reduction driving force to drive the reduction of CO_2 to CO. Notably, the conduction band edge of Pt/TiO_2-NB is located at −0.64 eV, which is 0.07 eV more negative than the −0.57 eV observed for Pt/TiO_2-NR. This negative shift indicates that Pt/TiO_2-NB possesses stronger conduction band reduction capability, facilitating the transfer of photo-generated electrons to CO_2 molecules and thereby significantly enhancing the photocatalytic activity for CO_2 reduction to CO [1,35]. The changes in the band structure of Pt/TiO_2-NB not only enable the capture of more visible light but also accelerate electron transfer. Based on scanning Kelvin probe (SKP) measurements and calculations, as shown in Figure 4d, the surface work functions of Pt/TiO_2-NB and Pt/TiO_2-NR are 5.71 eV and 5.76 eV, respectively, indicating that the two catalysts possess distinct electronic energy level structures on their surfaces, which may consequently affect the efficiency of photo-generated electron–hole (e^-–h^+) separation. The lower work function of Pt/TiO_2-NB ensures that electrons are more readily excited from the valence band (VB) and transferred to the surface [36]. Furthermore, the results indicate that the approximate Fermi level of Pt/TiO_2-NB is higher than that of Pt/TiO_2-NR. A higher Fermi level can enhance the self-induced electric field and surface band bending, thereby accelerating the transfer of photo-generated electrons to the surface, significantly reducing e^-–h^+ recombination, and markedly improving photocatalytic performance [37]. From the above results, it can be concluded that the higher the efficiency of photo-generated electron-hole separation, the better the light-driven effect; thus, the catalytic performance of Pt/TiO_2-NB is superior to that of Pt/TiO_2-NR.

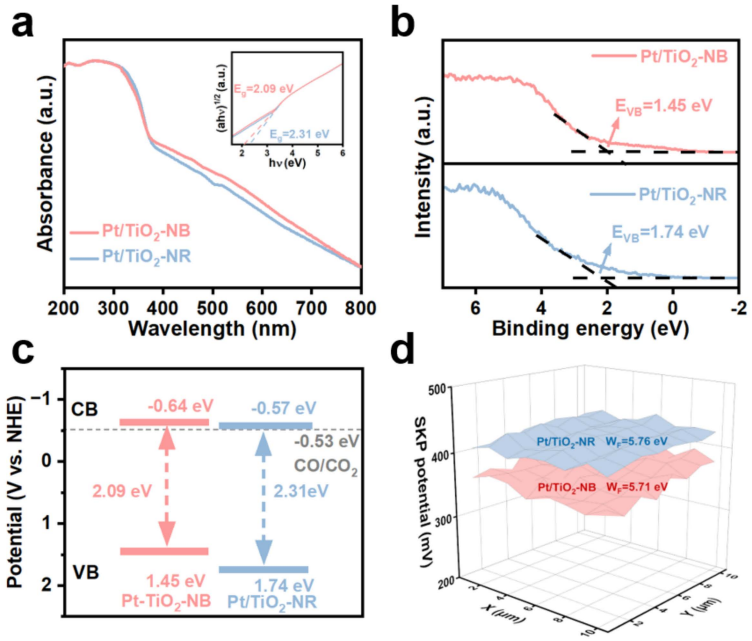

Figure 4. Characterization of Pt/TiO_2-NB and Pt/TiO_2-NR: (**a**) UV-Vis diffuse reflectance spectra (the corresponding optical bandgap diagrams are shown in the inset), (**b**) XPS valence band spectra, (**c**) band diagrams, and (**d**) scanning Kelvin probe maps.

2.3. Evaluation of the Light-Driven Performance of a Pt/TiO_2 Composite Catalyst in the Reverse Water-Gas Shift Reaction

The light-driven reaction was conducted in a self-built stainless steel continuous-flow reactor equipped with a quartz window at the top to ensure effective light transmis-

sion [9,38]. To evaluate the catalytic performance of this catalyst in the light-driven CO_2 hydrogenation reaction, the effect of different light intensities on reaction activity was systematically investigated, and the results are shown in Figure 5a. As the light intensity was gradually increased from 1.60 W/cm^2 to 3.20 W/cm^2, the CO_2 conversion rate showed a continuous upward trend, demonstrating a clear dependence on light intensity. Notably, within the range of light intensities tested, Pt/TiO_2-NB consistently exhibited superior catalytic activity compared to Pt/TiO_2-NR and Pt/TiO_2-P_{25}. At a light intensity of 2.80 W/cm^2, the CO_2 conversion rate of Pt/TiO_2-NB reached 33.60%, while those of Pt/TiO_2-NR and Pt/TiO_2-P_{25} were 26.17% and 22.53%, respectively, further validating the excellent light-driven CO_2 hydrogenation performance of Pt/TiO_2-NB. To further evaluate the intrinsic activity of the catalysts in the light-driven reverse water gas shift (RWGS) reaction, the apparent activation energy (E_a) of Pt/TiO_2-NB and Pt/TiO_2-NR was calculated using an Arrhenius plot. The results are shown in Figure 5b. The E_a for light-driven RWGS on the Pt/TiO_2-NB catalyst was 18.08 kJ mol^{-1}, which is lower than the E_a under Pt/TiO_2-NR catalytic conditions (24.44 kJ mol^{-1}). The Pt/TiO_2-NB catalyst exhibits a lower activation energy barrier for light-driven RWGS, which is conducive to the progression of the light-driven RWGS reaction. To comprehensively evaluate the catalytic performance potential of the two catalysts, this study investigated the effect of different gas-phase space velocities (GHSVs) on the CO_2 hydrogenation reaction performance under an irradiance of 2.50 W/cm^2. The experimental results are shown in Figure 5c. Under a GHSV as high as 600,000 mL·g^{-1}·h^{-1}, the CO production rates of Pt/TiO_2-NB and Pt/TiO_2-NR reached 57.03 mol·$g_{Pt}$$^{-1}$·h^{-1} and 51.98 mol·$g_{Pt}$$^{-1}$·h^{-1}, respectively. These results indicate that both catalysts exhibit excellent intrinsic catalytic activity, with Pt/TiO_2-NB performing slightly better than Pt/TiO_2-NR.

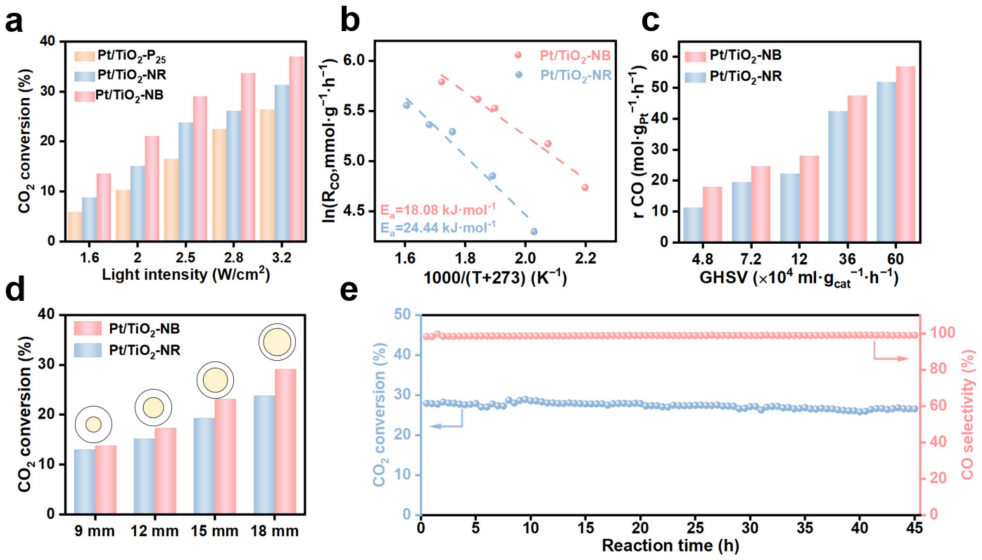

Figure 5. (**a**) CO_2 conversion rates of the Pt/TiO_2-NB, Pt/TiO_2-NR and Pt/TiO_2-P_{25} catalysts under different light intensities. (**b**) Arrhenius plots of CO production rates for the Pt/TiO_2-NB and Pt/TiO_2-NR catalysts under light-driven conditions. (**c**) CO production rates of the Pt/TiO_2-NB and Pt/TiO_2-NR catalysts at different GHSVs. (**d**) CO_2 conversion rates of the Pt/TiO_2-NB and Pt/TiO_2-NR catalysts at different effective illuminated areas. (**e**) Stability testing of the Pt/TiO_2-NB catalyst.

The above data fully demonstrate that both catalysts show good potential for industrial applications. Further investigation into the effect of irradiation area on the catalytic activity of the CO_2 hydrogenation reaction is shown in Figure 5d. Under a fixed catalyst loading, when the light intensity was 2.5 W/cm^2, increasing the irradiation spot radius from 9 mm to 18 mm resulted in a significant increase in CO_2 conversion rates for both

catalysts. On the Pt/TiO_2-NB catalyst, the conversion rate rose from 13.84% to 29.10%, while on the Pt/TiO_2-NR catalyst, it increased from 12.98% to 23.81%. This indicates that photo-generated electrons play a decisive role in CO_2 hydrogenation, and their promotional effect far exceeds what can be achieved by thermal catalysis alone. To evaluate the long-term stability of the Pt/TiO_2-NB catalyst in the light-driven reverse water gas shift reaction, this study conducted a 45 h continuous stability test, with the results shown in Figure 5e. Under an irradiance of 2.2 W/cm^2 and a space velocity of 72,000 $mL \cdot g^{-1} \cdot h^{-1}$, both the CO_2 conversion rate and CO selectivity of the catalyst remained stable, with no significant decline observed. The above results indicate that the Pt/TiO_2-NB catalyst not only exhibits excellent RWGS reactivity but also demonstrates good catalytic stability. To further investigate the structural evolution of the catalyst after long-term reaction, the post-reaction samples were characterized by SEM, XRD, and XPS (Figures S5–S8). The SEM images (Figure S5) show that the catalyst retains a uniform nanoparticle morphology, with no obvious large aggregates observed. The XRD pattern (Figure S6) indicates that the catalyst remains in the anatase phase, with no changes in the positions or relative intensities of the diffraction peaks compared to the pre-reaction sample. These results collectively confirm that the catalyst exhibits good structural integrity and phase stability, with no phase transformation occurring during the long-term reaction. Surface chemical state analysis of the post-reaction catalyst was performed using X-ray photoelectron spectroscopy (XPS), as shown in Figure S7. The O 1S XPS spectrum reveals that the oxygen vacancy-to-lattice oxygen ratio (O_V/O_L) on the post-reaction catalyst is 0.26, whereas the O_V/O_L ratio prior to the reaction was 0.25. This indicates that oxygen vacancies on the catalyst surface are well preserved even after prolonged reaction, demonstrating the catalyst's excellent surface structural stability. As shown in Figure S8 and Table S3, the Pt 4f XPS spectra reveal that there were no significant changes in the types or concentrations of Pt species before and after the reaction; Pt^{2+} remained the predominant species, indicating that this catalyst exhibits good structural stability and resistance to deactivation.

To investigate the contributions of light-driven and thermal-driven to the activity of the CO_2 hydrogenation reaction, photothermal cycling experiments were first conducted to systematically evaluate the CO_2 hydrogenation performance of the catalyst in a photothermal reactor. First, a light-driven reaction was carried out under an irradiance of 2.5 W/cm^2, followed immediately by a test under pure thermal conditions at the same temperature (i.e., the steady-state temperature reached during the light-initiated reaction) to compare the reaction activity under light-driven and thermal-driven conditions at the same temperature. The results of two repeated cycles (Figure 6a,b) confirmed the evolution of the catalyst's performance. The figures show that the activity of both catalysts reversibly recovered over the two cycles, and the catalyst structure remained stable. Furthermore, the light-driven activity of both catalysts was higher than their thermal-driven activity. The figures also indicate that the activity of the Pt/TiO_2-NB sample was higher than that of the Pt/TiO_2-NR sample.

To better distinguish the contributions of light-driven and thermal-driven mechanisms to the reaction, we further compared the CO_2 hydrogenation activity under these two conditions. As shown in Figure 6c,d, at the same temperature, the light-driven activity of both catalysts far exceeded their respective thermal-driven activities. On Pt/TiO_2-NB, under an irradiance of 2.50 W/cm^2 (catalyst surface temperature of 254 °C), the CO_2 conversion rate reached 29.10%. In contrast, the CO_2 conversion rate achieved by heating at the same temperature was only 2.75%, meaning that the conversion rate under the light-driven condition was approximately 10.58 times higher than that under the thermal-driven condition. On Pt/TiO_2-NR, under a light intensity of 2.5 W/cm^2 (catalyst surface temperature of 296 °C), the CO_2 conversion rate was 23.81%, whereas the result obtained by

heating at the same temperature was only 6.24%, meaning that the conversion rate under the light-driven condition is approximately 3.82 times that under the thermal-driven condition. These results indicate that the light-driven activity of both catalysts is significantly higher than their respective thermal-driven activities, suggesting that the photogenerated electron-hole pairs play a crucial role in CO_2 hydrogenation. In summary, the Pt/TiO_2-NB catalyst not only maintains long-term stability but also exhibits high selectivity and activity in the light-driven CO_2 process. It is suitable for industrial application. A performance comparison with previously reported catalysts (Figure 6e, Table S4) shows that the Pt/TiO_2-NB catalyst exhibits superior CO production rates at relatively low light intensities and catalyst surface temperatures, further demonstrating its exceptional catalytic performance in the RWGS reaction [1,4,5,38–43].

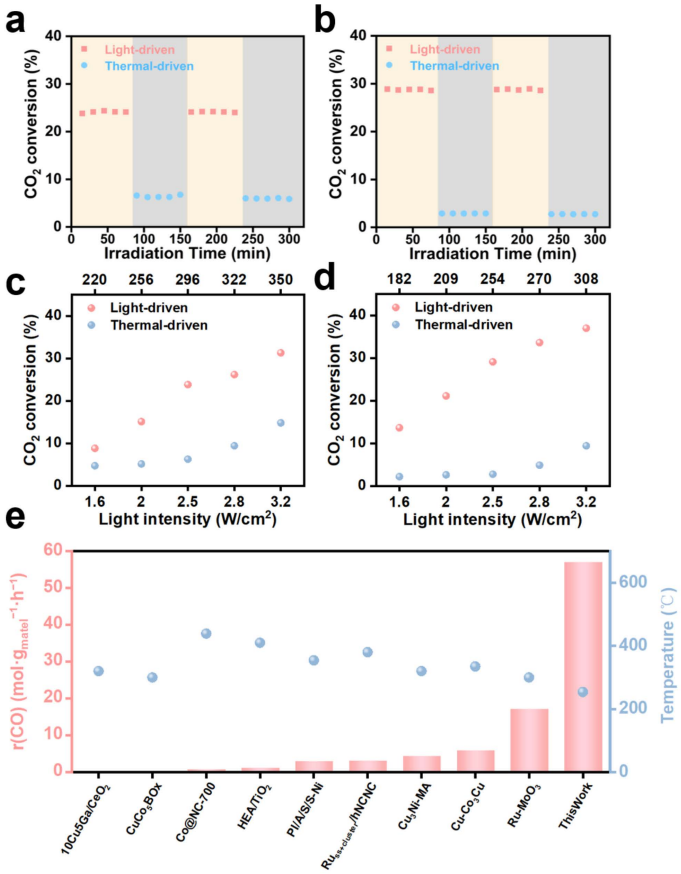

Figure 6. (**a**) Continuous spectra of light-driven and thermal-driven reactions for Pt/TiO_2-NR. (**b**) Continuous spectra of light-driven and thermal-driven reactions for Pt/TiO_2-NB. (**c**) CO_2 conversion rates of Pt/TiO_2-NR under different light intensities and corresponding temperatures (thermal-driven). (**d**) CO_2 conversion rates of Pt/TiO_2-NB under different light intensities and corresponding temperatures (thermal-driven). (**e**) The comparison of the light-driven RWGS reaction performance of different catalysts reported in the literature.

3. Materials and Methods

3.1. Chemicals

Titanium tetrachloride ($TiCl_4$, ≥99%), platinum (II) chloride hexahydrate ($H_2PtCl_6·6H_2O$), titanium (IV) hydroxide ($Ti(OH)_4$, >99%), ammonium chloride (NH_4Cl, >99%), ammonium sulfate ($(NH_4)_2SO_4$, ≥99%), and ammonia water ($NH_3·H_2O$) were purchased from Shanghai Aladdin Biochemical Technology Co., Ltd. (Shanghai, China). Ethanol (analytical grade) was purchased from Tianjin Fuyu Fine Chemical Co., Ltd. (Tianjin, China). All chemicals and materials were commercially available and not purified.

3.2. Methods

3.2.1. Synthesis of TiO_2 Precursor

At 0 °C, 6.6 mL of $TiCl_4$ was added dropwise to 20 mL of HCl (0.43 M). After stirring for 30 min, the solution was added dropwise to 50 mL of ammonia water (5.5 wt%) at room temperature. The pH was then adjusted to 6–7 using ammonia water, and the mixture was stirred for 2 h. The resulting precipitate was filtered and washed repeatedly until no Cl^- was detected, yielding $Ti(OH)_4$.

Under stirring at room temperature, 2.0 g of $Ti(OH)_4$ and 0.2 g of NH_4Cl were dispersed in 15 mL of ultrapure water. After thorough mixing, the mixture was transferred to a 50 mL autoclave, which was maintained at 180 °C for 24 h. The resulting white precipitate was collected and wash repeatedly with pure water and ethanol to obtain TiO_2-NB. Similarly, TiO_2-NR was prepared using 0.5 g of $(NH_4)_2SO_4$ instead of NH4Cl, with the precipitate washed in the same way.

3.2.2. Synthesis of Pt/TiO_2-NB and Pt/TiO_2-NR Catalysts

$H_2PtCl_6{\cdot}6H_2O$ was used as the Pt precursor. TiO_2 (1.0 g) and ultrapure H_2O (50 mL) were added together to a three-neck flask and mixed under stirring at 60 °C for 15 min. An appropriate amount of NH_3 (aq) was added to adjust the pH to 7–7.5, and the mixture was stirred at 60 °C for 1 h. The solid was then filtered, washed several times with H_2O, vacuum-dried at 60 °C for 12 h, and calcined at 400 °C in ambient air for 2 h. The resulting samples were placed in a tube furnace and heated to 400 °C at a heating rate of 5 °C per minute in a mixed H_2/N_2 atmosphere with a flow rate of 35 mL min^{-1}; they were then held at this temperature for 2 h for reduction. After reduction, the samples were designated Pt/TiO_2-NB and Pt/TiO_2-NR.

3.3. Characterization

Scanning Electron Microscopy (SEM) was performed using a ZEISS Sigma-500 field-emission scanning electron microscope (SEM, Carl Zeiss Microscopy GmbH, Oberkochen, Germany) to observe the sample morphology, using a test voltage of 5 kV.

Transmission Electron Microscopy (TEM) was performed using a JEOL-F200 transmission electron microscope (TEM, JEOL Ltd., Tokyo, Japan) to examine the sample morphology and structure, using an acceleration voltage of 200 kV.

X-ray Diffraction (XRD): X-ray diffraction (XRD) analysis was performed on a Bruker D8 Advance diffractometer (Bruker AXS GmbH, Karlsruhe, Germany), using an angular range of 20–80°.

Solid-State Electron Paramagnetic Resonance (EPR): The electron paramagnetic resonance (EPR) spectra of the samples were measured using a Bruker EMX plus spectrometer (Bruker BioSpin Corp., Billerica, MA, USA).

N_2 adsorption–desorption isotherm analysis: N_2 adsorption–desorption isotherms were collected using a TriStar II 3020 fully automated analyzer (Micromeritics Instrument Corp., Norcross, GA, USA).

UV-Vis absorption spectroscopy (UV-Vis): The UV-Vis absorption range of the materials was determined using a Shimadzu UV-2550 UV-Vis (Shimadzu Corp., Kyoto, Japan) diffuse reflectance spectrometer.

X-ray Photoelectron Spectroscopy (XPS): XPS is a technique used to characterize the valence state of elements on a sample's surface and its electronic structure. In this study, an ULTRA AXIS DLD photoelectron spectrometer manufactured by Shimadzu Corporation (Manchester, UK) was used for testing, with Al Kα radiation (hν = 1486.7 eV) serving as the test source.

Inductively Coupled Plasma Optical Emission Spectroscopy (ICP-OES): A Thermo Scientific iCAP 6300 (Thermo Fisher Scientific, Cambridge, UK) inductively coupled plasma optical emission spectrometer was used to determine the platinum loading on the catalyst.

Hydrogen Temperature-Programmed Reduction (H_2-TPR): The H_2-TPR experiments in this study were conducted using a PX200 multi-purpose gas adsorption analyzer from Tianjin Pengxiang (Tianjin, China). After pretreatment, 10 mg of the sample was weighed and heated to 400 °C at a heating rate of 5 °C/min in a N_2 atmosphere (27 mL/min), followed by reduction at this temperature for 1 h to remove impurities from the catalyst surface. After pretreatment, the sample was cooled to room temperature, then a N_2/H_2 gas mixture (H_2 flow rate: 3 mL/min; N_2 flow rate: 27 mL/min) was introduced, and the sample was heated to 600 °C at a rate of 10 °C/min while recording the signal.

For Hydrogen Temperature-Programmed Desorption (H_2-TPD), an equal mass of sample was taken and first exposed to a N_2/H_2 mixed gas (H_2 flow rate: 3 mL/min; N_2 flow rate: 27 mL/min). The sample was first pre-reduced: heated to 400 °C at a rate of 5 °C/min, reduced at this temperature for 1 h, and then allowed to cool naturally to room temperature. Then, the atmosphere was switched to an H_2 atmosphere (H_2 flow rate: 30 mL/min), which flowed for 1 h to allow the catalyst to adsorb H_2 to saturation. Next, the gas flow was switched to pure N_2 at the same flow rate of 30 mL/min and purged at room temperature for 30 min to remove any H_2 adsorbed on the sample surface. The catalyst surface was irradiated with a light source for 30 min. After cooling to room temperature, the sample was heated to 700 °C at a rate of 10 °C/min while recording the signal using the TCD.

For Carbon Dioxide Temperature-Programmed Desorption (CO_2-TPD) analysis, an equal mass of sample was taken and first exposed to a mixture of N_2/H_2 gas (H_2 flow rate: 3 mL/min; N_2 flow rate: 27 mL/min). The sample was first pre-reduced: heated to 400 °C at a rate of 5 °C/min, reduced at this temperature for 1 h, and then allowed to cool naturally to room temperature. Then, the atmosphere was switched to an CO_2 atmosphere (CO_2 flow rate: 30 mL/min), which flowed for 1 h to allow the catalyst to adsorb CO_2 to saturation. Next, the gas flow was switched to pure N_2 at the same flow rate of 30 mL/min and purged at room temperature for 30 min to remove any CO_2 adsorbed on the sample surface. The catalyst surface was irradiated with a light source for 30 min. After cooling to room temperature, the sample was heated to 700 °C at a rate of 10 °C/min while recording the signal using the TCD.

Scanning Kelvin Probe (SKP) Analysis: SKP analysis was performed using a Scottish-manufactured SKP5050 system (KP Technology Ltd., Wick, UK) in ambient air at atmospheric pressure, with a gold electrode serving as the reference electrode.

3.4. Catalytic Performance Evaluation

CO_2 hydrogenation activity was evaluated in a continuous-flow reactor with a circular quartz window (Shinsco Instrument Co., Ltd., Beijing, China) at atmospheric pressure. The light-driven reaction was conducted in a self-built stainless steel continuous-flow reactor equipped with a quartz window at the top to ensure effective light transmission. Initially, 40 mg of catalyst was uniformly coated onto a glass fiber sheet with a diameter of 18 mm. The catalyst-loaded glass fiber was then placed into the stainless-steel reactor, and a reaction gas containing CO_2 + H_2 (1:3) was introduced (48 mL/min). After 30 min, a full spectrum 300 W Xe lamp equipped with a collecting lens served as the light source to illuminate the catalyst through a quartz window on the top of the catalyst. The light intensity on the catalyst surface was measured using an optical power meter and the temperature of the catalyst surface was monitored using a thermocouple. The temperature of the reaction chamber was monitored using an inserted thermocouple (Figure S9). After stabilizing for

30 min, the exhaust gas was analyzed using an online gas chromatograph (Techcomp Scion 456C, Scion Instruments, Shanghai, China) equipped with a thermal conductivity detector (TCD) and a flame ionization detector (FID), with H_2 as the carrier gas. To prevent loss of the product, H_2O, due to water vapor condensation (which could affect measurement accuracy), the entire exhaust line was heated to 120 °C. CO and CO_2 were quantified using the TCD, while hydrocarbons (CH_4 and C_2–C_5) were detected using the FID. To ensure analytical accuracy, external standard calibration was performed before each experiment, and all gas concentrations were determined accordingly.

The CO_2 conversion, and the selectivity and production rate of CO at different gas hourly space velocities (GHSVs, 4.8–60 ($\times 10^4$) mL·g_{cat}^{-1}·h^{-1}) and light intensities (1.60–3.20 W/cm^2) were calculated according to the following equations:

$$CO_2 \text{ conversion } (\%) = \frac{[CO_2]_{in} - [CO_2]_{out}}{[CO_2]_{in}} \times 100\% \quad (1)$$

$$CO \text{ selectivity } (\%) = \frac{[CO]_{out}}{[CO]_{out} + [CH_4]_{out} + [C_xH_y]_{out}} \times 100\% \quad (2)$$

$$\text{Rate CO } \left(\text{mol}\cdot g_{Pt}^{-1}\cdot h^{-1}\right) = \frac{[CO]_{out}}{N_A \times m_{cat} \times L_{Pt} \times h} \quad (3)$$

where $[CO_2]_{in}$ and $[CO_2]_{out}$ represent the contents of CO_2 in the inlet gas and outlet gas, respectively. $[CO]_{out}$, $[CH_4]_{out}$, and $[C_xH_y]_{out}$ represent the contents of CO, CH_4 and hydrocarbons in the outlet gas. N_A is the Avogadro constant, m_{cat} is the catalyst loading mass, L_{Pt} is the mass fraction of Pt in the catalysts and h is the reaction time.

4. Conclusions

In summary, this study successfully synthesized Pt/TiO_2 catalysts with varying O_V concentrations by controlling the morphology of TiO_2, and systematically investigated the role of O_V in the light-driven reverse water-gas shift reaction. The results indicate that O_V concentration is a key factor determining catalyst performance. Structural characterization reveals that, compared to Pt/TiO_2-NR, Pt/TiO_2-NB is more conducive to H_2 reduction, resulting in a higher O_V concentration. Catalytic performance evaluation results show that under an irradiance of 2.5 W/cm^2 and a space velocity of 600,000 mL·g^{-1}·h^{-1}, the CO production rates of the Pt/TiO_2-NB catalyst reached 57.03 mol·g_{Pt}^{-1}·h^{-1}. Furthermore, the catalyst maintained excellent catalytic stability during continuous operation for 45 h, demonstrating good potential for practical application.

Supplementary Materials: The following supporting information can be downloaded at: https://www.mdpi.com/article/10.3390/catal16070620/s1, Figure S1: BJH pore size distribution curve of Pt/TiO_2-NB; Figure S2: BJH pore size distribution curve of Pt/TiO_2-NR; Figure S3. H_2-TPR Curves for Pt/TiO_2-NB and TiO_2; Figure S4: CO_2-TPD Curves for Pt/TiO_2-NB and Pt/TiO_2-NR; Figure S5: SEM images of Pt/TiO_2-NB after the light-driven RWGS reaction; Figure S6: XRD pattern of Pt/TiO_2-NB after the light-driven RWGS reaction; Figure S7: O 1S XPS spectrum of the Pt/TiO_2–NB catalyst after the light-driven RWGS reaction; Figure S8: Pt 4f XPS spectrum of the Pt/TiO_2–NB catalyst following the light-driven RWGS reaction; Figure S9: Photo diagram of a light-driven reaction setup: (a) illumination mode; (b) catalyst loading method in the reaction cell; Table S1: Parameters Related to N_2 Adsorption and Desorption for Pt/TiO_2-NB and Pt/TiO_2-NR; Table S2: ICP-OES Results for Pt/TiO_2-NB and Pt/TiO_2-NR; Table S3. Pt valence states and content in Pt/TiO_2-NB and RWGS-Pt/TiO_2-NB as determined by XPS; Table S4. Performance Comparison of Photothermal Catalysts.

Author Contributions: Conceptualization, L.F.; methodology, J.L.; software, J.S.; validation, Y.J., X.J. and Q.Z.; formal analysis, S.S.; investigation, C.Z.; resources, J.L.; data curation, L.F. and Q.Z.; writing—original draft preparation, L.F.; writing—review and editing, J.L.; visualization, L.F., Y.J., X.J.

and Q.Z.; supervision, J.S.; project administration, J.L.; funding acquisition, J.L. All authors have read and agreed to the published version of the manuscript.

Funding: This work was financially supported by the Natural Science Foundation of Heilongjiang Province (PL2025B027), the Program for Young Talents of Basic Research in Universities of Heilongjiang Province (YQJH2025187), and the "Double First-Class" Discipline Collaborative Innovation Achievement Project of Heilongjiang Province (LJGXCG2025-P23).

Data Availability Statement: All the data are contained within the article.

Conflicts of Interest: The authors declare no conflicts of interest.

References

1. Chu, D.D.; Xu, M.K.; Zou, Y.J.; Xing, C.; Sun, D.; Ling, L. In Situ Dynamic Structural Changes of Ruthenium-Loaded MoO_3 for Photothermal Catalytic CO_2 Reduction. *ACS Catal.* **2025**, *15*, 11266–11276. [CrossRef]
2. Wu, J.; Li, K.; An, S.; Yan, S.; Liu, J.; Song, C.; Guo, X. An S-scheme heterojunction of single Ni sites decorated ultrathin carbon nitride and Bi_2WO_6 for highly efficient photothermal CO_2 conversion to syngas. *Appl. Catal. B Environ. Energy* **2024**, *347*, 123822. [CrossRef]
3. Bai, K.P.; Chen, W.P.; Cui, M.D.; Zheng, Y.Z. Photocatalytic Reduction of CO_2 to CO in 100%: The Synergistic Effect of Nickel and Europium in Heterometallic Clusters. *Angew. Chem. Int. Ed. Engl.* **2025**, *64*, e202511126. [CrossRef] [PubMed]
4. Xiong, H.; Ji, X.; Mao, K.; Dong, Y.; Cai, L.; Chen, A.; Chen, Y.; Hu, C.; Ma, J.; Wan, J.; et al. Light-Driven Reverse Water Gas Shift Reaction with 1000-H Stability on High-Entropy Alloy Catalysts. *Adv. Mater.* **2024**, *36*, e2409689. [CrossRef] [PubMed]
5. Ma, J.; Yu, J.; Chen, G.; Bai, Y.; Liu, S.; Hu, Y.; Al-Mamun, M.; Wang, Y.; Gong, W.; Liu, D.; et al. Rational Design of N-Doped Carbon-Coated Cobalt Nanoparticles for Highly Efficient and Durable Photothermal CO_2 Conversion. *Adv. Mater.* **2023**, *35*, e2302537. [CrossRef] [PubMed]
6. Zhao, Z.; Doronkin, D.E.; Ye, Y.; Grunwaldt, J.-D.; Huang, Z.; Zhou, Y. Visible light-enhanced photothermal CO_2 hydrogenation over Pt/Al_2O_3 catalyst. *Chin. J. Catal.* **2020**, *41*, 286–293. [CrossRef]
7. Ahmed, S.; Khan, M.K.; Kim, J. Revolutionary advancements in carbon dioxide valorization via metal-organic framework-based strategies. *Carbon Capture Sci. Technol.* **2025**, *15*, 100405. [CrossRef]
8. Liu, J.; Huang, Z.; Zheng, X.; Nasir, M.S.; Wang, D.; Wang, P.; Li, J.; Li, Y.; Zhu, L.; Wang, X.; et al. Ru-RuO_2 Coordinated with Si-Supported GaN Nanowires for Light-Driven Simultaneous Activation of CO_2 and H_2 to Achieve Exceptional Reverse Water-Gas Shift Reaction. *Angew. Chem. Int. Ed. Engl.* **2025**, *64*, e202511886. [CrossRef] [PubMed]
9. Wan, X.; Li, Y.; Chen, Y.; Ma, J.; Liu, Y.A.; Zhao, E.D.; Gu, Y.; Zhao, Y.; Cui, Y.; Li, R.; et al. A nonmetallic plasmonic catalyst for photothermal CO_2 flow conversion with high activity, selectivity and durability. *Nat. Commun.* **2024**, *15*, 1273. [CrossRef] [PubMed]
10. Bobadilla, L.F.; Santos, J.L.; Ivanova, S.; Odriozola, J.A.; Urakawa, A. Unravelling the Role of Oxygen Vacancies in the Mechanism of the Reverse Water-Gas Shift Reaction by OperandoDRIFTS and Ultraviolet-Visible Spectroscopy. *ACS Catal.* **2018**, *8*, 7455–7467. [CrossRef]
11. Wan, X.Y.; Zhao, Y.L.; Li, Y.F.; Ma, J.; Gu, Y.; Liu, C.; Luo, Y.; Yang, G.; Cui, Y.; Liu, D.; et al. Tailoring Oxygen Vacancies with Atomically Dispersed Cu Sites for Stable and Efficient Photothermal CO_2 Conversion. *Angew. Chem.-Int. Ed.* **2025**, *64*, e202505244. [CrossRef] [PubMed]
12. Ou, H.; Ning, S.; Zhu, P.; Chen, S.; Han, A.; Kang, Q.; Hu, Z.; Ye, J.; Wang, D.; Li, Y. Carbon Nitride Photocatalysts with Integrated Oxidation and Reduction Atomic Active Centers for Improved CO_2 Conversion. *Angew. Chem. Int. Ed. Engl.* **2022**, *61*, e202206579. [CrossRef] [PubMed]
13. Ren, Y.; Si, Y.; Du, M.; You, C.; Zhang, C.; Zhu, Y.H.; Sun, Z.; Huang, K.; Liu, M.; Duan, L.; et al. Photothermal Synergistic Effect Induces Bimetallic Cooperation to Modulate Product Selectivity of CO_2 Reduction on Different CeO_2 Crystal Facets. *Angew. Chem. Int. Ed. Engl.* **2024**, *63*, e202410474. [CrossRef] [PubMed]
14. Shi, Z.; Yang, L.; Lu, Z.; Han, Q.; Wu, L.; Wang, L.; Xiong, Y.; Ye, J.; Zou, Z.; Zhou, Y. Comprehensive Insight into Indium Oxide-Based Catalysts for CO_2 Hydrogenation: Thermal, Photo, and Photothermal Catalysis. *Adv. Funct. Mater.* **2024**, *34*, 2409904. [CrossRef]
15. Pang, Q.Q.; Zhong, X.H.; Yan, W.S.; Ma, H.; Ren, H.; Song, L.; Lv, Z.; Li, L.; Chen, C.; Wang, H.; et al. Role of percentage of {001} crystal facets in TiO_2 supports toward the water-gas shift reaction over Au-TiO_2catalysts. *Chem. Eng. J.* **2022**, *446*, 137010. [CrossRef]
16. Xiang, Q.; Lv, K.; Yu, J. Pivotal role of fluorine in enhanced photocatalytic activity of anatase TiO_2 nanosheets with dominant (001) facets for the photocatalytic degradation of acetone in air. *Appl. Catal. B Environ.* **2010**, *96*, 557–564. [CrossRef]

17. Wei, Z.; Yue, X.; Ji, Y.; Mu, H.; Wu, L.; Chen, S.; Yi, G.; Chang, Y.; Wang, C.; Juodkazis, S.; et al. Nanoarchitecture design for improved photocatalytic performance: A case study of titania mesocrystals modified with noble metals. *Appl. Catal. B Environ. Energy* **2025**, *383*, 126112. [CrossRef]
18. Yu, S.; Wang, Z.; Xie, Y.; Li, G.; Li, Y. Single-atom Electronic Bridge Facilitates Cascade Electron Transfer From Encapsulated Polyoxometalate to Metal-Organic Framework for Efficient Photocatalytic CO_2 Conversion. *Angew. Chem. Int. Ed. Engl.* **2026**, *65*, e24558. [CrossRef] [PubMed]
19. Li, B.; Zhang, X.; Chen, M.; Huang, X.; Fang, X.; Yang, Y.; Li, Y.; Ma, B.; Ding, Y. Multichannel charge transfer mediated by polyoxometalate loaded SnS_2 wrapped Te nanostructures for efficient photocatalytic CO_2 reduction. *Appl. Catal. B Environ. Energy* **2025**, *377*, 125509. [CrossRef]
20. Li, R.G.; Weng, Y.X.; Zhou, X.; Wang, X.; Mi, Y.; Chong, R.; Han, H.; Li, C. Achieving overall water splitting using titanium dioxide-based photocatalysts of different phases. *Energy Environ. Sci.* **2015**, *8*, 2377–2382. [CrossRef]
21. Chen, S.L.; Li, D.; Liu, Y.; Huang, W. Morphology-dependent defect structures and photocatalytic performance of hydrogenated anatase TiO_2 nanocrystals. *J. Catal.* **2016**, *341*, 126–135. [CrossRef]
22. Selcuk, S.; Selloni, A. Facet-dependent trapping and dynamics of excess electrons at anatase TiO_2 surfaces and aqueous interfaces. *Nat. Mater.* **2016**, *15*, 1107–1112. [CrossRef] [PubMed]
23. Li, D.; You, R.; Yang, M.; Liu, Y.; Qian, K.; Chen, S.; Cao, T.; Zhang, Z.; Tian, J.; Huang, W. Morphology-Dependent Evolutions of Sizes, Structures, and Catalytic Activity of Au Nanoparticles on Anatase TiO_2 Nanocrystals. *J. Phys. Chem. C* **2019**, *123*, 10367–10376. [CrossRef]
24. Fu, C.; Li, F.; Zhang, J.; Li, D.; Qian, K.; Liu, Y.; Tang, J.; Fan, F.; Zhang, Q.; Gong, X.Q.; et al. Site Sensitivity of Interfacial Charge Transfer and Photocatalytic Efficiency in Photocatalysis: Methanol Oxidation on Anatase TiO_2 Nanocrystals. *Angew. Chem. Int. Ed. Engl.* **2021**, *60*, 6160–6169. [CrossRef] [PubMed]
25. Chen, Z.Y.; Liang, L.; Yuan, H.; Liu, H.; Wu, P.; Fu, M.; Wu, J.; Chen, P.; Qiu, Y.; Ye, D.; et al. Reciprocal regulation between support defects and strong metal-support interactions for highly efficient reverse water gas shift reaction over Pt/TiO_2 nanosheets catalysts. *Appl. Catal. B Environ.* **2021**, *298*, 120507. [CrossRef]
26. Hoang, S.; Berglund, S.P.; Hahn, N.T.; Bard, A.J.; Mullins, C.B. Enhancing Visible Light Photo-oxidation of Water with TiO_2 Nanowire Arrays via Cotreatment with H_2 and NH_3: Synergistic Effects between Ti^{3+} and N. *J. Am. Chem. Soc.* **2012**, *134*, 3659–3662. [CrossRef] [PubMed]
27. Wei, Z.-W.; Wang, H.-J.; Zhang, C.; Xu, K.; Lu, X.-L.; Lu, T.-B. Reversed Charge Transfer and Enhanced Hydrogen Spillover in Platinum Nanoclusters Anchored on Titanium Oxide with Rich Oxygen Vacancies Boost Hydrogen Evolution Reaction. *Angew. Chem.-Int. Ed.* **2021**, *60*, 16622–16627. [CrossRef] [PubMed]
28. Feng, D.Y.; Dong, Y.B.; Zhang, L.L.; Ge, X.; Zhang, W.; Dai, S.; Qiao, Z.-A. Holey Lamellar High-Entropy Oxide as an Ultra-High-Activity Heterogeneous Catalyst for Solvent-free Aerobic Oxidation of Benzyl Alcohol. *Angew. Chem.-Int. Ed.* **2020**, *59*, 19503–19509. [CrossRef] [PubMed]
29. Ma, K.; Zhao, S.; Dou, M.; Ma, X.; Dai, C. Enhancing the Stability of Methanol-to-Olefins Reaction Catalyzed by SAPO-34 Zeolite in the Presence of CO_2 and Oxygen-Vacancy-Rich $ZnCeZrO_x$. *ACS Catal.* **2023**, *14*, 594–607. [CrossRef]
30. Xu, C.Y.; Huang, W.H.; Li, Z.; Deng, B.; Zhang, Y.; Ni, M.; Cen, K. Photothermal Coupling Factor Achieving CO_2 Reduction Based on Palladium-Nanoparticle-Loaded TiO_2. *Acs Catal.* **2018**, *8*, 6582–6593. [CrossRef]
31. Han, Q.; Wu, C.B.; Jiao, H.M.; Xu, R.; Wang, Y.; Xie, J.; Guo, Q.; Tang, J. Rational Design of High-Concentration Ti^{3+} in Porous Carbon-Doped TiO_2 Nanosheets for Efficient Photocatalytic Ammonia Synthesis. *Adv. Mater.* **2021**, *33*, 2008180. [CrossRef] [PubMed]
32. Speck, F.D.; Paul, M.T.Y.; Ruiz-Zepeda, F.; Gatalo, M.; Kim, H.; Kwon, H.C.; Mayrhofer, K.J.J.; Choi, M.; Choi, C.H.; Hodnik, N.; et al. Atomistic Insights into the Stability of Pt Single-Atom Electrocatalysts. *J. Am. Chem. Soc.* **2020**, *142*, 15496–15504. [CrossRef] [PubMed]
33. Kang, X.; Liu, J.; Xie, Y.; Wang, D.; Liu, Q.; Yu, P.; Tian, C.; Fu, H. Pt single atoms in oxygen vacancies boost reverse water-gas shift reaction by enhancing hydrogen spillover. *Sci. China Mater.* **2024**, *67*, 3579–3588. [CrossRef]
34. Zhang, W.; Wang, H.Z.; Jiang, J.W.; Sui, Z.; Zhu, Y.; Chen, D.; Zhou, X. Size Dependence of Pt Catalysts for Propane Dehydrogenation: From Atomically Dispersed to Nanoparticles. *ACS Catal.* **2020**, *10*, 12932–12942. [CrossRef]
35. Qu, J.; Wang, Y.; Mu, X.; Hu, J.; Zeng, B.; Lu, Y.; Sui, M.; Li, R.; Li, C. Determination of Crystallographic Orientation and Exposed Facets of Titanium Oxide Nanocrystals. *Adv. Mater.* **2022**, *34*, e2203320. [CrossRef] [PubMed]
36. Zhang, X.C.; Hu, W.Y.; Zhang, K.F.; Wang, J.; Sun, B.; Li, H.; Qiao, P.; Wang, L.; Zhou, W. Ti^{3+}Self-Doped Black TiO_2 Nanotubes with Mesoporous Nanosheet Architecture as Efficient Solar-Driven Hydrogen Evolution Photocatalysts. *Acs Sustain. Chem. Eng.* **2017**, *5*, 6894–6901. [CrossRef]
37. Jiang, B.J.; Tang, Y.Q.; Qu, Y.; Wang, J.-Q.; Xie, Y.; Tian, C.; Zhou, W.; Fu, H. Thin carbon layer coated Ti^{3+}-TiO_2 nanocrystallites for visible-light driven photocatalysis. *Nanoscale* **2015**, *7*, 5035–5045. [CrossRef] [PubMed]

38. Liu, S.; Wang, X.; Chen, Y.; Li, Y.; Wei, Y.; Shao, T.; Ma, J.; Jiang, W.; Xu, J.; Dong, Y.; et al. Efficient Thermal Management with Selective Metamaterial Absorber for Boosting Photothermal CO_2 Hydrogenation under Sunlight. *Adv. Mater.* **2024**, *36*, e2311957. [CrossRef] [PubMed]
39. Deng, B.; Song, H.; Peng, K.; Li, Q.; Ye, J. Metal-organic framework-derived Ga-Cu/CeO_2 catalyst for highly efficient photothermal catalytic CO_2 reduction. *Appl. Catal. B Environ.* **2021**, *298*, 120519. [CrossRef]
40. Wang, J.; Li, S.; Zhao, J.; Liu, K.; Jiang, B.; Li, H. Boron-doped Cu-Co catalyst boosting charge transfer in photothermal carbon dioxide hydrogenation. *Appl. Catal. B Environ. Energy* **2024**, *352*, 124045. [CrossRef]
41. Wang, Z.J.; Zhou, Y.M.; Ni, W.K.; Li, J.; Yue, X.; Zhang, Z.; Dai, W.; Fu, X. Stable hydroxyl-anchored CuNi nanocatalysts from CuNiMgAl-LDH thermal reduction for efficient photothermal CO_2 conversion. *Nat. Commun.* **2025**, *16*, 10497. [CrossRef] [PubMed]
42. Sun, Z.X.; Zhou, C.; Chen, Z.; Zeng, Y.; Sun, T.; Dong, X.; Yang, L.; Wang, X.; Wu, Q.; Huang, H.; et al. Decoupling Activity-Selectivity Trade-off in Photothermal Catalytic CO_2 Hydrogenation: A Hydrogen Spillover-Assisted Dual-Site Synergy Mechanism. *Angew. Chem. Int. Ed. Engl.* **2025**, *64*, e202508090. [CrossRef] [PubMed]
43. Gu, Y.; Zhao, E.D.; Wan, X.; Ma, J.; Liu, D.; Xiong, Y. Reaction-Induced Phase Engineering of CuCo Nanoparticles for Enhanced Photothermal CO_2 Hydrogenation. *Adv. Mater.* **2026**, *38*, e15661. [CrossRef] [PubMed]